

# Channel-Selected Stratified Nested Cross-Validation for Clinically Relevant EEG-Based Parkinson's Disease Detection

Nicholas R. Rasmussen, Rodrigue Rizk, Longwei Wang, Arun Singh, KC Santosh

**Abstract**—The early detection of Parkinson's disease remains a critical challenge in clinical neuroscience, with electroencephalography offering a non-invasive and scalable pathway toward population-level screening. While machine learning has shown promise in this domain, many reported results suffer from methodological flaws, most notably patient-level data leakage, inflating performance estimates and limiting clinical translation. To address these modeling pitfalls, we propose a unified evaluation framework grounded in nested cross-validation and incorporating three complementary safeguards: (i) patient-level stratification to eliminate subject overlap and ensure unbiased generalization, (ii) multi-layered windowing to harmonize heterogeneous EEG recordings while preserving temporal dynamics, and (iii) inner-loop channel selection to enable principled feature reduction without information leakage. Applied across three independent datasets with a heterogeneous number of channels, a convolutional neural network trained under this framework achieved 80.6% accuracy and demonstrated state-of-the-art performance under held-out population block testing, comparable to other methods in the literature. This performance underscores the necessity of nested cross-validation as a safeguard against bias and as a principled means of selecting the most relevant information for patient-level decisions, providing a reproducible foundation that can extend to other biomedical signal analysis domains.

**Index Terms**—Channel Selection, Nested Cross-Validation, Clinical Stratification, Parkinson's Disease Detection, Electroencephalography (EEG), Signal Processing

## I. INTRODUCTION

Parkinson's disease (PD) is the second most common neurodegenerative disorder, affecting over 10 million people worldwide and imposing a growing socioeconomic burden [1]. Its progressive course—marked by motor dysfunction, cognitive decline, and reduced quality of life—makes early detection and intervention a critical priority [2], [3]. Yet current clinical diagnosis is largely based on overt motor symptoms, which typically emerge only after substantial dopaminergic neuron loss [2], [3]. This delay highlights the importance of identifying prodromal biomarkers, such as REM sleep behavior disorder, olfactory impairment, and subtle motor irregularities, which often precede clinical diagnosis by years [2]. Detecting early PD could enable interventions when therapies are effective [2].

Advances in biomedical signal acquisition have created new opportunities for non-invasive monitoring of these prodromal and progressive symptoms [4]. Among available modalities, electroencephalography (EEG) is particularly promising: it is portable, relatively inexpensive, and offers millisecond-level temporal resolution of neural dynamics [5]. Compared to imaging techniques such as MRI or PET, which provide high spatial resolution but are costly and

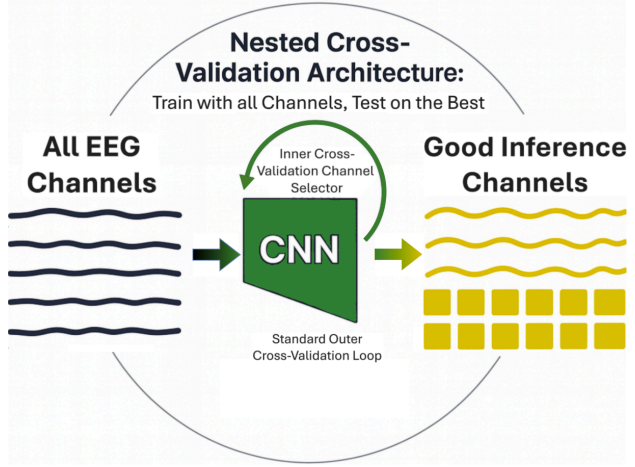


Fig. 1. The nested cross-validation architecture addresses the challenge of high-dimensional EEG data by starting with all channels and systematically reducing to the most informative. The inner loop selects channels contributing most to inference, while the outer loop validates this choice without bias. This principled “many-to-best” reduction is dataset-, channel-, and model-agnostic, yielding results that are more efficient, generalizable, and interpretable.

less accessible, EEG enables scalable, repeated assessments that are well-suited for longitudinal monitoring [5], [6]. This combination of accessibility and temporal precision positions EEG as a strong candidate for early PD biomarker discovery.

In parallel, machine learning (ML) and deep learning (DL) methods show strong potential for extracting subtle biomarkers from high-dimensional biomedical data [7]. A wide range of neural architectures have been explored for biosignal analysis: recurrent neural networks (RNNs) and long short-term memory (LSTM) models capture temporal dependencies in sequential data [8]; transformer-based models leverage self-attention to model long-range interactions across time and frequency; and graph neural networks (GNNs) exploit the spatial topology of EEG electrode layouts to learn structured representations [9]. Despite these advances, convolutional neural networks (CNNs) remain a principled starting point for EEG analysis. When applied to short-time Fourier transform (STFT) spectrograms, CNNs exploit partial shift-invariance that complements the local stationarity of the STFT, enabling robust feature extraction without handcrafted preprocessing [10], [11], [12]. This synergy has consistently delivered state-of-the-art performance across diverse signal domains, including PD detection, where CNN-based or hybrid pipelines frequently report accuracies exceeding 95% [13]. Moreover, CNN architectures are nat-

urally extensible to multimodal fusion: EEG inputs can be paired with bio-signal sensor data through parallel branches converging in shared layers, allowing integrated biomarker discovery without redesigning the core model [14].

Many reported successes in EEG-based PD detection are undermined by methodological flaws, most notably data leakage and dataset heterogeneity. Leakage arises in two primary forms: *temporal leakage*, where overlapping windows from the same recording are split across training and test sets, and *subject leakage*, where data from the same patient appears in both folds. In both cases, models risk memorizing idiosyncratic traits rather than learning disease-relevant features, inflating performance and eroding clinical validity [15]. Surveys of PD classification studies further highlight that EEG research often employs ambiguous patient-level stratification, if it is applied at all [16]. Population block testing offers a partial safeguard, yet its scope is limited, as models may still overfit to the unique characteristics of a single cohort. These concerns are compounded by the heterogeneity of public EEG datasets: channel counts range from high-density 64-channel caps to sparse consumer devices, and acquisition hardware differs in sampling rate, electrode placement, and preprocessing pipelines. Methods tuned to one configuration often fail to transfer across others, creating a significant reproducibility barrier. Collectively, these challenges underscore the need for architectures that prevent leakage, generalize across populations, and robustly reduce high-dimensional signals to the most informative subset, independent of dataset or recording setup.

To address these challenges, we propose a *nested cross-validation framework* for robust EEG analysis (Figure 1). The outer loop enforces patient-level stratification to eliminate leakage, while the inner loop selects the most informative channels, reducing dimensionality without sacrificing clinically relevant signals. A multi-layered windowing strategy integrates recordings of varying length, sampling rate, and hardware, enabling consistent evaluation across heterogeneous datasets. By design, the framework is dataset, channel, and model-agnostic, positioning it as a blueprint for reproducible EEG-based biomarker discovery. Together, these components yield generalizable performance estimates and clinically meaningful early PD detection results.

Our contributions are threefold:

- 1) A model-agnostic nested cross-validation framework with stratification, windowing, and inner-loop channel selection to prevent leakage, harmonize datasets, and reduce dimensionality.
- 2) Empirical evidence that patient-level leakage and narrow cohort blocking inflate EEG-based PD detection performance and undermine clinical validity.
- 3) Demonstration that learned representations align with canonical EEG frequency bands, yielding interpretable models that achieve 0.806 accuracy across datasets.

Looking forward, this framework provides a foundation for accelerating clinical translation: it enables reproducible biomarker validation across heterogeneous cohorts, supports integration with multimodal data streams such as EMG and

wearable sensors, and lays the groundwork for scalable digital health pipelines capable of monitoring neurodegenerative disease progression in real-world settings.

## II. RELATED WORK AND METHODOLOGICAL PITFALLS

A growing body of research has applied ML techniques to the early detection of PD using EEG, EMG, and other biosignal modalities. Several studies have reported high classification accuracies, often exceeding 85%, suggesting strong potential for clinical translation [17], [18]. However, closer inspection reveals that many of these works rely on evaluation protocols that do not stratify data at the patient level. Instead, temporal windows from the same subject are distributed across both training and test sets, creating a form of *data leakage*. This allows models to exploit subject-specific idiosyncrasies rather than learning generalizable disease markers, thereby inflating performance estimates [15], [19], [20], [21].

Beyond this central issue, several additional pitfalls recur across the literature. The small sample sizes typical of PD datasets magnify overfitting risks, as even a few misallocated subjects can distort reported outcomes [20]. Reported performance is also often reduced to accuracy, which obscures clinically relevant trade-offs; complementary metrics such as sensitivity, specificity, ROC-AUC, and calibration curves provide a more reliable assessment [22], [23]. Preprocessing choices—including channel selection, filtering, and artifact removal—introduce further variability and can bias results when hyperparameters are tuned on overlapping data [19], [24]. Although nested cross-validation is widely used in other domains for ensembling [19] and hyperparameter optimization [25], it can be applied in PD detection to quantify variability across patient-level hold-out sets and channel configurations. In heterogeneous settings with rare events, neglecting such stability checks risks overconfident claims of deployment readiness [21]. Finally, no existing PD studies attempt non-harmonized cross-dataset validation (e.g., Iowa vs. San Diego), leaving open whether models trained on one population can generalize to others with different acquisition protocols or demographics.

DL approaches have also been explored for PD detection, but many inherit the same evaluation flaws. For instance, [26] applied convolutional neural networks to EEG recordings of patients and controls with ambiguous enforcement of subject-independent splits, leaving the reported performance difficult to interpret. Likewise, [13] presented hybrid convolutional models with seemingly strong results, yet overlapping patient data across folds assuredly inflated accuracy estimates. Comparable practices appear in other studies [16], [27], [28], [21], where non-stratified cross-validation or single-block testing at the population level introduce systematic bias. Collectively, these works illustrate how even sophisticated methods can yield misleading outcomes when evaluation fails to guard against leakage and overfitting.

A more recent example is the GAN-Enhanced Generalizable Model for EEG-Based Detection of Parkinson’s

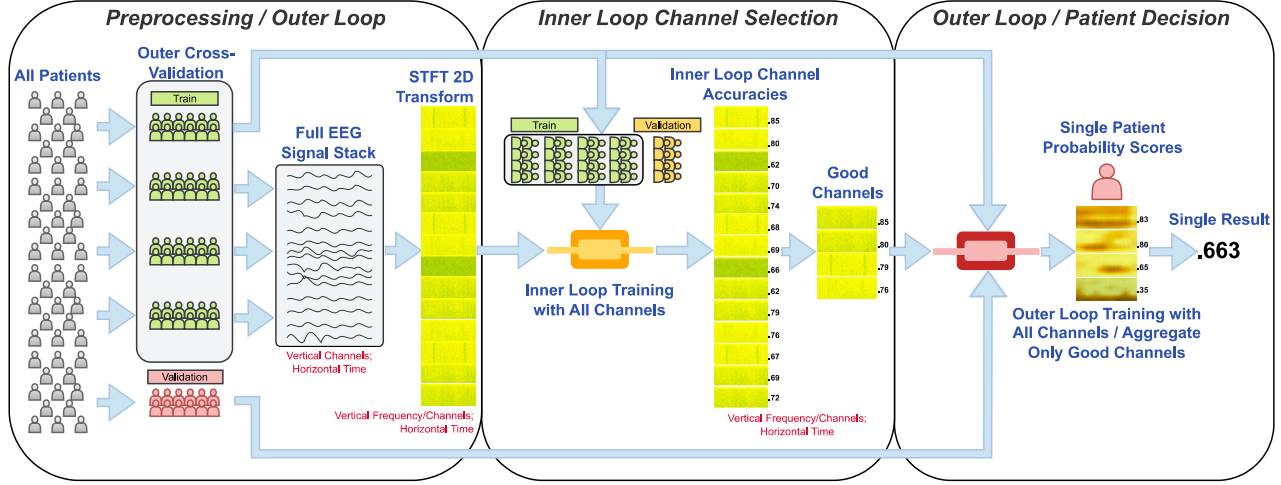


Fig. 2. Suggested Workflow for EEG Channel Selection Modeling: Subjects are represented by raw EEG time-series, which are transformed into spectrograms via short-time Fourier transform. An inner cross-validation loop trains a model to estimate per-channel performance, retaining only the most informative electrodes. These selected channels are reintegrated into the outer training and validation framework, where the final model is trained. Predictions are then aggregated into a single patient-level probability, providing a concise outcome measure.

Disease (GEPD) [29], which reported roughly 85% accuracy using generative augmentation. While advancing cross-dataset generalization, its reliance on a single 90/10 split and train-on-Iowa/test-on-UNM configuration—without patient-level aggregation—raises concerns. Similar protocols, including the reverse train/test setup [16], [21], risk tuning models to population-specific artifacts, producing unstable and inflated performance estimates. Furthermore, GEPD discarding non-matching EEG channels across datasets limits clinical applicability. More broadly, generative augmentation itself can amplify inherent biases if synthetic samples reproduce population-specific artifacts rather than disease-relevant features, underscoring the need for careful validation [30].

In contrast, our design emphasizes rigorous evaluation by integrating three public datasets without discarding viable channels, applying five-fold stratified cross-validation with patient grouping, and reporting outcomes at the patient level. These protocols mitigate overfitting to dataset artifacts and yield more reliable estimates of generalization, a critical requirement for biomedical applications. Our approach also advances interpretability, where prior studies treat neural networks as black boxes, we provide band-level explanations of EEG features, illuminating which spectral components drive predictions. Thus, methodological robustness and transparent feature attribution demonstrates that competitive performance can be achieved without data leakage or singular validations, while also enhancing trust and clinical relevance.

### III. PROPOSED NESTED CROSS-VALIDATION ARCHITECTURE

Our framework integrates preprocessing, windowing, and feature extraction with a *nested cross-validation* design that enforces patient-level separation, supports principled channel selection, and, when desired, incorporates CNN-based band alignment for interpretability. The overall workflow is illustrated in Figure 2 and narrated throughout this section.

#### A. Preprocessing

All preprocessing steps are intended to normalize EEG signals within target frequency bands for our nested cross-validation framework. Let  $s_m(t)$  denote the raw EEG signal for patient  $p_m$ , sampled at original frequency  $f_{\text{orig}}$ . Each signal was resampled to a common rate of  $f_s = 64$  Hz to preserve oscillatory activity in the Beta (13–30 Hz) and Theta (4–8 Hz) bands. The resampled signal  $\tilde{s}_m(t)$  was standardized to zero mean and unit variance,  $\mathbf{z}_m(t) = \frac{\tilde{s}_m(t) - \mu_m}{\sigma_m}$ , where  $\mu_m$  and  $\sigma_m$  are the mean and standard deviation of  $\tilde{s}_m(t)$ . Each standardized trace was then normalized to unit amplitude,  $\hat{s}_m(t) = \frac{\mathbf{z}_m(t)}{\max_t |\mathbf{z}_m(t)|}$ . For each subject  $p_m$ , the aligned EEG arrays  $\hat{s}_m(t)$  were stored in a DataFrame with metadata (ID, session, diagnosis, file name). Thus, ensuring reproducibility, subject-level traceability, and partitioning within outer cross-validation folds, preventing leakage from the outset.

To ensure comparability across datasets, we incorporated a channel harmonization step. Let  $\mathcal{C} = \{c_1, c_2, \dots, c_C\}$  denote the full set of electrodes, where  $|\mathcal{C}|$  corresponds to the number of channels in the Iowa dataset. Channels were first partitioned into anatomical regions,  $\mathcal{C} = \mathcal{C}_{\text{frontal}} \cup \mathcal{C}_{\text{fronto-central}} \cup \mathcal{C}_{\text{central}} \cup \dots \cup \mathcal{C}_{\text{occipital}}$ , with each subset  $\mathcal{C}_r$  preserving spatial contiguity. Within each region, electrodes were ordered according to standard EEG conventions:

$$c \in \mathcal{C}_r = \begin{cases} \text{left hemisphere,} & \text{if index is odd,} \\ \text{midline,} & \text{if label ends in } z, \\ \text{right hemisphere,} & \text{if index is even.} \end{cases} \quad (1)$$

After ordering, each channel was assigned a unique integer index  $\pi : \mathcal{C} \rightarrow \{0, 1, \dots, C-1\}$ , such that  $\pi(c)$  reflects its position in the harmonized left-to-right, anterior-to-posterior sequence. This mapping provided a consistent spatial template across datasets, enabling reproducible alignment of electrodes to model inputs and ensuring that subsequent channel

selection operated on harmonized, regionally structured arrays. To accommodate datasets with incomplete coverage, any channel  $c \in \mathcal{C}$  absent from a given recording was zero-padded at its corresponding index  $\pi(c)$ . This ensured that all input arrays conformed to the full Iowa-based template, preserving spatial structure while maintaining compatibility across heterogeneous datasets.

### B. Cross-Validation Schema

As illustrated in Figure 2, we adopt a patient-stratified nested cross-validation design where the outer loop estimates generalization to unseen patients and the inner loop supports model selection and channel pruning. Both loops use *StratifiedGroupKFold* with patient identifiers from our DataFrame’s metadata as grouping variables, ensuring all samples  $\mathcal{W}_m$  from a patient  $p_m$  are confined to either training or testing folds. This structure prevents patient and temporal leakage while preserving class balance, whereby nesting hyperparameter tuning and channel selection within the inner loop maintains unbiased outer evaluations.

### C. Windowing and Feature Extraction

To define the data segments used in the cross-validation schema, we employed a windowing strategy tailored to split the ‘Full EEG Signal Stack’ of each patient into channel separated spectrograms, as depicted in Figure 2, which vary in length and recording conditions. With sampling rate  $f_s = 64$  Hz, the outer window length was set to  $L_w = 16,384$  samples, corresponding to  $\frac{16,384}{f_s} \approx 256$  s. Shorter signals were zero-padded, and longer signals segmented into overlapping windows with hop size  $H_w = \frac{L_w}{4} = 4,096$  samples. Within each window, we computed the short-time Fourier transform (STFT). For a discrete-time signal  $\mathbf{w}[n] \in \mathbb{R}^T$ , the STFT is

$$\text{STFT}(i, f) = \sum_{k=0}^{L-1} \mathbf{w}[bi+k] \cdot \mathbf{x}[k] \cdot e^{-j2\pi kf/L}, \quad (2)$$

where  $L$  is the analysis window length,  $b$  the hop size,  $\mathbf{x}[k]$  the window function,  $f$  the frequency bin index, and  $i$  the time frame index. This yields a complex-valued matrix of size  $N \times L$ , with  $N = \lfloor \frac{T}{b} \rfloor$ ,  $\Delta f = \frac{f_s}{L}$ . We used  $n_{\text{fft}} = 256$  and  $h = 64$  samples, producing spectrograms with  $F = \frac{n_{\text{fft}}}{2} = 128$  frequency bins,  $T = \frac{L_w}{h} = \frac{16,384}{64} = 256$  time bins. Each EEG channel was thus represented as  $(F \times T \times 1) = (128 \times 256 \times 1)$ , normalized and converted to decibel scale. This procedure expands each patient’s EEG into multiple channel separated spectrograms, increasing training sample size and enabling finer-grained decisions while maintaining stable computational demands.

### D. Channel Selection

As highlighted in the ‘Inner Loop Channel Selection’ stage of Figure 2, channel selection is embedded within the nested cross-validation schema to address the high dimensionality of EEG recordings, where  $C \in \{32, 64\}$  active electrodes capture distinct neural activity. For each outer fold’s training set, spectrograms from all active channels  $\{c_1, c_2, \dots, c_C\}$

are passed through the CNN, and per-channel accuracies  $a_{c,f}$  are recorded on each inner-fold validation subset  $f \in \{1, \dots, F\}$ . These fold-wise accuracies are then accumulated and averaged to obtain a stability-adjusted score for each channel where only the active channels for each patient are accumulated into their respective average,

$$\bar{a}_c = \frac{1}{F} \sum_{f=1}^F a_{c,f}. \quad (3)$$

Channels are ranked by  $\bar{a}_c$ , and the top subset  $\mathcal{C}^* \subseteq \{c_1, \dots, c_C\}$  is retained for evaluation in the outer fold; channel selection occurs in the inner loop, ensuring dimensionality reduction is guided by cross-validated evidence rather than outer-fold outcomes, while in the outer loop the CNN is retrained on the full channel set and the inner loop identifies electrodes most reliable for inference, maintaining strict separation to preserve patient-level validity.

### E. CNN Band-Level Alignment

As illustrated in the ‘Single Patient Probability Scores’ stage of Figure 2, we optionally employ the Adaptable Resolution Pooling Network (ARP-N), a convolutional model trained within both inner and outer loops of the pipeline. ARP-N transforms variable-sized spectrograms into consistent square feature maps through convolutional blocks, batch normalization, dropout, and specialized pooling, followed by a dense sigmoid output. For each channel  $c$ , the STFT spectrogram  $\mathbf{X}_c \in \mathbb{R}^{F \times T}$  with  $F = 128$  frequency bins and  $T = 256$  time bins is adaptively pooled to  $\mathbf{Z}_c \in \mathbb{R}^{8 \times 8}$ . Along the frequency axis,  $F = 128 \rightarrow F' = 8$ , thus spanning

$$\Delta f' = \frac{32 \text{ Hz}}{8} = 4 \text{ Hz}. \quad (4)$$

This resolution aligns directly with canonical EEG bands—[0–4] Hz (Delta), [4–8] Hz (Theta), [8–12] Hz (Alpha), and [12–30] Hz (Beta, subdivided)—embedding neuroscientific conventions into the architecture itself. In practice, ARP-N highlights spectral-temporal regions most indicative of Parkinson’s, providing implicit band-level interpretability while reducing computational cost and improving generalization across heterogeneous datasets.

### F. Patient-Level Evaluation

As shown in Figure 2 under ‘Patient Decision’, evaluation is performed at the patient-level to reflect clinical use cases. Each patient  $p_m \in \mathcal{P}$  contributes a set of windowed spectrograms  $\mathcal{W}_m$ , and the model produces window-level probabilities  $\hat{y}_{mi}$ . These are aggregated by simple averaging,

$$\hat{y}_m = \frac{1}{|\mathcal{W}_m|} \sum_{i=1}^{|\mathcal{W}_m|} \hat{y}_{mi}, \quad (5)$$

yielding a single prediction per patient. This procedure ensures that performance metrics correspond to generalization across distinct individuals rather than across overlapping signal segments, thereby aligning the evaluation with the outer cross-validation design and providing clinically meaningful estimates of model utility.

## IV. EXPERIMENTS AND RESULTS

We evaluated our framework through a series of controlled experiments spanning multiple datasets, metrics, and model configurations. The following subsections detail the datasets used, evaluation criteria, baseline comparisons, and implementation choices, followed by analyses of model performance (Table I), aggregation strategies (Table II), and interpretability via Grad-CAM visualizations (Figure 3).

### A. Datasets

We combined three independent EEG dataset's resting state eyes closed subsets to assess robustness and generalizability: (i) *Iowa*, 64-channel BioSemi ActiveTwo recordings; (ii) *University of New Mexico (UNM)*, multi-session 64-channel EEG from PD patients and controls; and (iii) *San Diego*, clinical 32-channel EEG representing hardware variability. All signals were aligned to our canonical montage set forth in III-A, with missing channels zero-filled to preserve indexing. This harmonization enabled cross-dataset evaluation without architectural modification.

### B. Evaluation Metrics

With the dataset approximately balanced at the patient level, we report accuracy, area under the ROC curve (AUC), precision, and recall without adjustments. These metrics capture overall correctness, threshold discrimination, and the trade-off between false positives and negatives, providing a robust evaluation under balanced conditions.

### C. Implementation and Reproducibility

All experiments were implemented in Python with tensorflow/keras. Outputs were stored in DataFrames and logged to CSVs to ensure reproducibility. Training employed Adamax with an exponential learning-rate schedule, early stopping, and checkpointing. Crucially, reproducibility is anchored by the nested cross-validation channel selection routine (Algorithm 1), which formalizes how channels are chosen and evaluated across folds. Readers are referred to Algorithm 1 for the full specification.

### D. Baselines

Table I summarizes performance across three evaluation paradigms. The first, *No Stratification*, trains without patient-level separation, permitting temporal and subject leakage; we also include results from Lee et al. [13] and Wu et al. [21], who used a comparable setup. The second, *Single-Population Blocking*, reflects models optimized for a single site or cohort; our I-4-C model is shown alongside Anjum et al. [16] and Zhang et al. [29], both evaluated under similar conditions. The third, *Stratified Cross-Validation*, is our proposed framework, enforcing patient-level separation across folds. Here, the *All-Channel* model uses all electrodes, while reduced-channel variants (1-, 2-, 4-, 8-, 16-Channel) demonstrate principled channel selection. These comparisons reveal inflated performance under non-stratified or population-blocked designs and more clinically relevant estimates with stratified cross-validation.

---

### Algorithm 1 Nested Cross-Validation Channel Selection

---

**Require:** Full dataset  $X_{data}$ , labels  $y_{data}$ , patient groups  $G_{data}$ , channel indices  $C_{data}$ , parameters  $\theta$ , number of inner folds  $K$ , shared memory slots  $L$

**Ensure:** Best channel subset  $\mathcal{C}^*$ , performance across folds

- 1: Initialize results list  $\mathcal{R} \leftarrow \emptyset$
- 2: Initialize channel score dictionary  $\mathcal{S}[ch] \leftarrow \emptyset$
- 3: **for** all outer fold  $(X_{train}, X_{test})$  **do**
- 4:     Store data into shared memory slots  $L$
- 5:     Initialize inner cross-validation with  $K$  splits
- 6:     **for**  $k \leftarrow 1$  to  $K$  **do**
- 7:         Split into inner-train and inner-validation sets:  
 $(X_{tr}^{(k)}, y_{tr}^{(k)}, G_{tr}^{(k)}, C_{tr}^{(k)})$   
 $(X_{val}^{(k)}, y_{val}^{(k)}, G_{val}^{(k)}, C_{val}^{(k)})$
- 8:         Store data into shared memory slots  $L$
- 9:          $\theta \leftarrow \text{runTrain}(L, \text{inner} = \text{True})$
- 10:          $M \leftarrow \text{runChan}(L, \theta)$
- 11:         **for** all channel  $ch$  in  $M$  **do**
- 12:             Append accuracy  $M[\text{Acc}][ch]$  to  $\mathcal{S}[ch]$
- 13:         **end for**
- 14:     **end for**
- 15:     Compute channel accuracy:  $\bar{a}[ch] \leftarrow \text{mean}(\mathcal{S}[ch])$
- 16:      $\mathcal{C}^* \leftarrow \text{Top-}m \text{ channels by } \bar{a}[ch]$
- 17:     Store  $\mathcal{C}^*$  in  $L$
- 18:      $\theta \leftarrow \text{runTrain}(L, \text{inner} = \text{False})$
- 19:     Record results restricted to  $(\theta, \mathcal{C}^*)$  into  $\mathcal{R}$
- 20: **end for**
- 21: Aggregate results across folds into dataframe  $D$
- 22: Compute averages per configuration:  $\bar{D} \leftarrow \text{mean}(D)$
- 23: **return**  $\mathcal{C}^*, \bar{D}$

---

### E. Comparative Analysis

The first paradigm, *No Stratification*, achieved the highest apparent performance in our experiments (Acc = .985, AUC = .986, Prec = .995, Rec = .978), with Lee et al. [13] and Wu et al. [21] reporting better metrics. However, these results reflect data leakage rather than genuine generalization since patient overlap across folds inflates performance, along with near-zero variance that further signals overfitting. While the other architecture slightly outperforms ours under flawed evaluation, such comparisons are not meaningful: without patient-level separation, performance cannot be interpreted as evidence of clinical utility.

Under the *Single-Population Blocking* paradigm, our 4-Channel model decisively outperformed prior approaches. In the Iowa-blocked evaluation, it achieved Acc = .929, AUC = .929, Prec = .875, and Rec = 1.00—substantially higher than the mid-.80s accuracies reported by Anjum et al. [16], Zhang et al. [29], and Wu et al. [21] under comparable blocked designs. This margin underscores the strength of our feature extraction and channel selection strategy, even when models are tuned to a single dataset. However, such blocked evaluations can be misleading: by restricting training and testing to the same population, they risk inflating performance through site-specific artifacts rather than genuine

disease-relevant features. Although population block testing offers a partial safeguard, it remains narrow, as models may still overfit to the unique characteristics of a single cohort. These limitations highlight why cross-validation with patient-level separation is essential for establishing true generalizability and clinical validity.

Our framework is the first to provide clinically realistic estimates of generalization on heterogeneous EEG channel datasets by enforcing patient-level separation through *Stratified Cross-Validation*. Within this rigorous setting, the *4-Channel* configuration delivered the strongest overall trade-off, achieving  $\text{Acc} = .806 \pm .092$  and  $\text{Rec} = .801 \pm .134$  while maintaining stable precision ( $.785 \pm .159$ ). The *2-Channel* model offered balanced but slightly weaker performance ( $\text{Acc} = .774$ ,  $\text{AUC} = .797$ ), whereas the *8-Channel* variant favored precision ( $.819 \pm .108$ ) at the expense of recall ( $.706 \pm .157$ ). By contrast, the *16-Channel* model underperformed across all metrics, suggesting that excessive electrodes introduce redundancy or noise. These results demonstrate not only the robustness of our channel selection strategy but also the importance of evaluating models under stratified, patient-level cross-validation, where inflated performance from site-specific artifacts is minimized and true generalization can be assessed.

Taken together, these results reveal that inflated scores often stem from temporal or patient leakage rather than true predictive ability, and that best-case performance within a single dataset can mask poor generalization under heterogeneous conditions. By contrast, our stratified framework enforces patient-level separation, yielding more conservative but clinically meaningful estimates. Moderate channel configurations consistently provided the most reliable balance, whereas both minimal and excessive channel counts degraded performance, underscoring the value of principled selection in the inner loop. Overall, findings highlight the need of stratification and the unique contribution of our framework in aligning evaluation with clinical deployment.

#### F. Patient-Level Aggregation Ablation

Table II presents an ablation of aggregation strategies for patient-level decisions in our nested cross-validation framework. Across all configurations, *Mean* and *Median* aggregation consistently produced the most balanced outcomes, reinforcing their reliability for patient-level evaluation. The *4-Channel* models performed best overall, with both rules yielding strong accuracy and recall, while *2-Channel* models also improved on the baseline. Other strategies showed less stability: *Majority* performed competitively but leaned toward higher precision, Geometric Mean (*GMean*) was slightly weaker yet serviceable, and *Max* and *Min* proved unreliable—either overemphasizing precision at the cost of recall or collapsing under outliers. Importantly, the *Iowa Blocked Test* followed this same general trend: *Mean*, *Median*, and *Majority* aggregation produced the strongest and most stable results, while *Min* and *Max* underperformed.

Overall, these findings show that aggregation is not a secondary detail but a central design choice that directly

TABLE I  
PERFORMANCE COMPARISON UNDER DIFFERENT STRATIFICATION STRATEGIES AND CHANNEL SUBSETS.

Model	Acc	$\sigma$	AUC	$\sigma$	Prec	$\sigma$	Rec	$\sigma$
<b>No Stratification</b>								
Wu [21]	1.00	NA	1.00	NA	1.00	NA	1.00	NA
Lee [13]	.992	NA	.992	NA	.989	NA	.994	NA
Ours	.985	0	.986	.001	.995	.008	.978	.008
<b>Single-Population Blocking</b>								
<b>I-4C (Ours)</b>	.929	NA	.929	NA	.875	NA	1.00	NA
Anjum [16]	.857	NA	.852	NA	.857	NA	.857	NA
Wu [21]	.857	NA	.841	NA	.916	NA	.786	NA
Zhang [29]	.843	NA	NA	NA	.840	NA	.840	NA
<b>Stratified Cross-Validation</b>								
All-Channel	.715	.070	.738	.102	.711	.091	.759	.131
1-Channel	.752	.124	.797	.130	.777	.158	.714	.136
2-Channel	.774	.107	.797	.104	.785	.159	.742	.125
<b>4-Channel</b>	.806	.092	.799	.067	.785	.159	.801	.134
8-Channel	.767	.117	.752	.154	.819	.108	.706	.157
16-Channel	.748	.092	.753	.143	.793	.112	.703	.154

TABLE II  
ABLATION OF AGGREGATION STRATEGIES FOR PATIENT-LEVEL DECISION MAKING UNDER DIFFERENT CHANNEL CONFIGURATIONS.

Method	Acc	$\sigma$	AUC	$\sigma$	Prec	$\sigma$	Rec	$\sigma$
<b>Single-Population Blocking</b>								
I-4C GMean	.821	NA	.913	NA	.846	NA	.786	NA
<b>I-4C Majority</b>	.929	NA	.944	NA	.875	NA	1.00	NA
I-4C Max	.607	NA	.957	NA	.560	NA	1.00	NA
I-4C Mean	.893	NA	.944	NA	.824	NA	1.00	NA
<b>I-4C Median</b>	.929	NA	.944	NA	.875	NA	1.00	NA
I-4C Min	.571	NA	.832	NA	1.00	NA	.143	NA
<b>Stratified Cross-Validation</b>								
All GMean	.685	.103	.734	.095	.608	.153	.777	.143
All Majority	.715	.070	.738	.102	.711	.091	.759	.131
All Max	.633	.135	.731	.098	.867	.130	.615	.145
All Mean	.707	.084	.738	.102	.693	.115	.751	.147
All Median	.715	.070	.734	.101	.711	.091	.759	.131
All Min	.573	.147	.694	.116	.310	.230	.790	.262
2C GMean	.785	.092	.806	.086	.785	.159	.766	.130
2C Majority	.766	.106	.797	.104	.807	.123	.721	.130
2C Max	.766	.106	.814	.101	.807	.123	.721	.130
2C Mean	.774	.107	.797	.104	.785	.159	.742	.125
2C Median	.774	.107	.801	.104	.785	.159	.742	.125
2C Min	.749	.091	.806	.087	.721	.187	.750	.126
4C GMean	.756	.091	.796	.052	.689	.165	.777	.160
<b>4C Majority</b>	.801	.084	.799	.067	.829	.099	.762	.141
4C Max	.765	.100	.816	.072	.829	.099	.711	.129
<b>4C Mean</b>	.806	.092	.799	.067	.785	.159	.801	.134
<b>4C Median</b>	.797	.082	.826	.052	.807	.123	.770	.133
4C Min	.717	.095	.748	.074	.608	.183	.750	.199

shapes clinical validity. Robust rules such as *Mean* and *Median* not only stabilize fold-to-fold variance but also preserve the sensitivity–specificity balance needed for screening contexts. Conversely, unstable rules amplify the same risks seen with poor stratification or excessive channel counts; namely, poor generalization. Thus, careful aggregation complements stratified cross-validation and principled channel selection, forming our framework for reliable patient-level evaluation.

#### G. Grad-CAM Interpretability Visualization

Grad-CAM overlays in Figure 3 revealed that the network consistently emphasized the *theta band* (4–8 Hz) across channels, with secondary contributions from *alpha* (8–12 Hz) and *beta* (12–30 Hz) ranges. In several cases, the model highlighted recurrent *theta–alpha structures* with rhythmic fluctu-

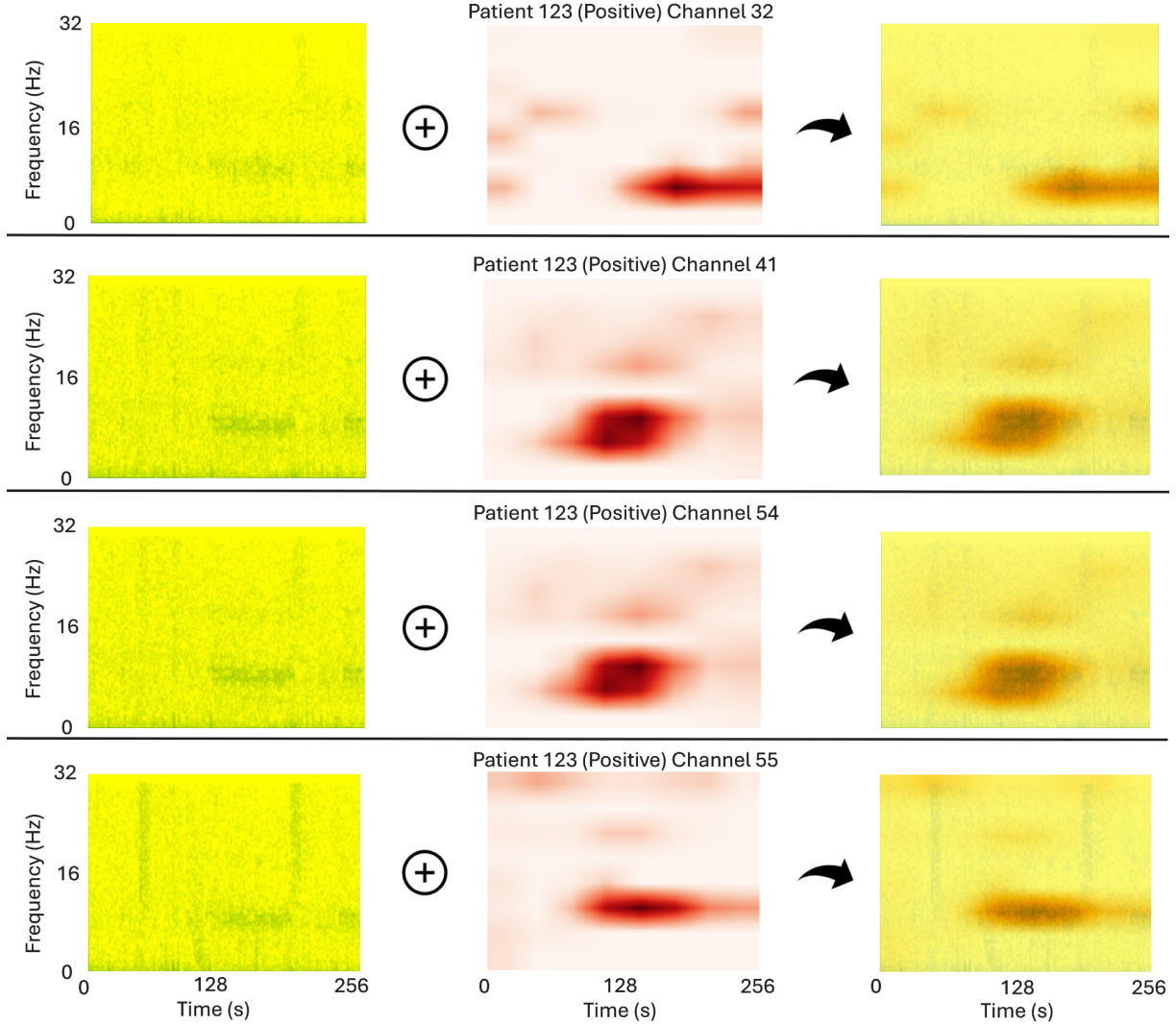


Fig. 3. Grad-CAM overlays for Patient 123 highlight consistent band-level focus. Each row shows one EEG channel (32, 41, 54, 55), progressing from spectrogram (yellow-green) to Grad-CAM heatmap (red) to overlay. The model emphasizes recurrent theta activity (4–8 Hz), with secondary attention in alpha (8–12 Hz) and occasional beta (12–30 Hz). These theta–alpha patterns broaden and narrow rhythmically, producing a pulsing appearance distinct from noise or artifacts. While edge effects (e.g., aliasing, zero-padding) sometimes attract attention, the dominant focus remains on physiologically plausible oscillations, underscoring both the strengths and limits of convolutional interpretability

ations in spectral bandwidth, producing a pulsing appearance distinct from artifacts. While the CNN occasionally attended to *processing artifacts* (e.g., zero-padding or aliasing), the dominant focus remained within physiologically meaningful bands; therefore aligning with canonical oscillatory rhythms suggesting learned representations are discriminative and *neurophysiologically interpretable*. The frequency-specific spatially distributed activations across channels further indicate that the network captured *cross-channel dependencies* rather than isolated channel effects.

This pattern aligns with prior EEG studies in PD, which report consistent alterations in theta and beta. For example, increased *frontal theta activity* and impaired *beta desynchronization* during lower-limb movement have been linked to motor deficits and freezing of gait (FOG) in PD patients [31]. Complementary work using *linear predictive coding* shows

PD patients exhibit not only theta and beta abnormalities but also *reduced alpha power*, distinguishing them from healthy controls [16]. Thus, our Grad-CAM results suggest that ARP-N is *aligned with clinical research*. By discretizing the 0–32 Hz spectrum into 4 Hz bins, the network is structurally matched to canonical EEG bands, encouraging band-level representations that Grad-CAM makes visible, thereby strengthening confidence in interpretability.

## V. CONCLUSION

We introduced a nested cross-validation framework for early detection of PD from EEG, designed as a reproducible and generalizable response to common methodological pitfalls. By harmonizing three independent datasets (Iowa, UNM, San Diego) into a consistent montage, we established a foundation for cross-site evaluation. Patient stratification

in the outer loop prevented data leakage, while multi-layered windowing preserved temporal structure and enabled uniform processing of heterogeneous recordings. The inner loop enabled principled channel selection, reducing dimensionality and improving generalization by emphasizing the most informative electrodes. Patient-level aggregation, particularly mean and median, further reinforced clinical reliability. Collectively, these components show nested cross-validation as a principled model-agnostic solution to leakage, dimensionality, and heterogeneity challenges that have historically inflated performance. Beyond PD, our architecture offers a reproducible framework for EEG and ML studies emphasizing scientific rigor, transparency, and clinical applicability.

#### ACKNOWLEDGMENTS

The author acknowledges Microsoft Copilot for assistance with grammar and structural edits, contextual extrapolation in the results section, and figure preparation with extensive human input [32]. All core ideas, analyses, and interpretations are the author's own based on previous literature and experimental analysis, as cited in the manuscript.

#### REFERENCES

- [1] Y. Li, Z. Lv, Y. Dai, L. Yu, L. Zhang, K. Wang, and P. Hu, "The global, regional, and national burden of parkinson's disease in 204 countries and territories, 1990–2021: a systematic analysis for the global burden of disease study 2021," *BMC Public Health*, vol. 25, no. 1, p. 3047, 2025.
- [2] B. R. Bloem, M. S. Okun, and C. Klein, "Parkinson's disease," *The Lancet*, vol. 397, no. 10291, pp. 2284–2303, 2021.
- [3] L. V. Kalia and A. E. Lang, "Parkinson's disease," *The lancet*, vol. 386, no. 9996, pp. 896–912, 2015.
- [4] C. Moreau, T. Rouaud, D. Grabi, I. Benatru, P. Remy, A.-R. Marques, S. Drapier, L.-L. Mariani, E. Roze, D. Devos *et al.*, "Overview on wearable sensors for the management of parkinson's disease," *npj Parkinson's Disease*, vol. 9, no. 1, p. 153, 2023.
- [5] C. M. Michel and D. Brunet, "Eeg source imaging: a practical review of the analysis steps," *Frontiers in neurology*, vol. 10, p. 325, 2019.
- [6] R. Cassani, M. Estarellas, R. San-Martin, F. J. Fraga, and T. H. Falk, "Systematic review on resting-state eeg for alzheimer's disease diagnosis and progression assessment," *Disease markers*, vol. 2018, no. 1, p. 5174815, 2018.
- [7] S. Steyaert, M. Pizurica, D. Nagaraj, P. Khandelwal, T. Hernandez-Boussard, A. J. Gentles, and O. Gevaert, "Multimodal data fusion for cancer biomarker discovery with deep learning," *Nature machine intelligence*, vol. 5, no. 4, pp. 351–362, 2023.
- [8] Y. Roy, H. Berville, I. Albuquerque, A. Gramfort, T. H. Falk, and J. Faubert, "Deep learning-based electroencephalography analysis: a systematic review," *Journal of neural engineering*, vol. 16, no. 5, p. 051001, 2019.
- [9] E. Vafaei and M. Hosseini, "Transformers in eeg analysis: A review of architectures and applications in motor imagery, seizure, and emotion classification," *Sensors*, vol. 25, no. 5, p. 1293, 2025.
- [10] N. Hatami, Y. Gavet, and J. Debayle, "Classification of time-series images using deep convolutional neural networks," in *Tenth international conference on machine vision (ICMV 2017)*, vol. 10696. SPIE, 2018, pp. 242–249.
- [11] A. Chaman and I. Dokmanic, "Truly shift-invariant convolutional neural networks," in *Proceedings of the IEEE/CVF Conference on Computer Vision and Pattern Recognition*, 2021, pp. 3773–3783.
- [12] F. Hlawatsch and G. Boudreaux-Bartels, "Linear and quadratic time-frequency signal representations," *IEEE Signal Processing Magazine*, vol. 9, no. 2, pp. 21–67, 1992.
- [13] S. Lee, R. Hussein, R. Ward, Z. J. Wang, and M. J. McKeown, "A convolutional-recurrent neural network approach to resting-state eeg classification in parkinson's disease," *Journal of neuroscience methods*, vol. 361, p. 109282, 2021.
- [14] H.-T. Lee, M. Shim, X. Liu, H.-R. Cheon, S.-G. Kim, C.-H. Han, and H.-J. Hwang, "A review of hybrid eeg-based multimodal human-computer interfaces using deep learning: applications, advances, and challenges," *Biomedical Engineering Letters*, pp. 1–32, 2025.
- [15] T. Torres Moral, A. Sanchez-Niubo, A. Monistrol-Mula, C. Gerardi, R. Banzi, P. Garcia, J. Demotes-Mainard, J. M. Haro, and P. Group, "Methods for stratification and validation cohorts: a scoping review," *Journal of Personalized Medicine*, vol. 12, no. 5, p. 688, 2022.
- [16] M. F. Anjum, S. Dasgupta, R. Mudumbai, A. Singh, J. F. Cavanagh, and N. S. Narayanan, "Linear predictive coding distinguishes spectral eeg features of parkinson's disease," *Parkinsonism & related disorders*, vol. 79, pp. 79–85, 2020.
- [17] M. Aljalal, S. A. Aldosari, K. AlSharabi, A. M. Abdurraqeem, and F. A. Alturki, "Parkinson's disease detection from resting-state eeg signals using common spatial pattern, entropy, and machine learning techniques," *Diagnostics*, vol. 12, no. 5, p. 1033, 2022.
- [18] S. K. Khare, V. Bajaj, and U. R. Acharya, "Detection of parkinson's disease using automated tunable q wavelet transform technique with eeg signals," *Biocybernetics and Biomedical Engineering*, vol. 41, no. 2, pp. 679–689, 2021.
- [19] D. R. Roberts, V. Bahn, S. Ciuti, M. S. Boyce, J. Elith, G. Guillera-Arroita, S. Hauenstein, J. J. Lahoz-Monfort, B. Schröder, W. Thuiller *et al.*, "Cross-validation strategies for data with temporal, spatial, hierarchical, or phylogenetic structure," *Ecography*, vol. 40, no. 8, pp. 913–929, 2017.
- [20] J. Racine, "Consistent cross-validatory model-selection for dependent data: hv-block cross-validation," *Journal of econometrics*, vol. 99, no. 1, pp. 39–61, 2000.
- [21] H. Wu, J. Qi, E. Purwanto, X. Zhu, P. Yang, and J. Chen, "Multi-scale feature and multi-channel selection toward parkinson's disease diagnosis with eeg," *Sensors*, vol. 24, no. 14, p. 4634, 2024.
- [22] T. Saito and M. Rehmsmeier, "The precision-recall plot is more informative than the roc plot when evaluating binary classifiers on imbalanced datasets," *PloS one*, vol. 10, no. 3, p. e0118432, 2015.
- [23] E. W. Steyerberg, A. J. Vickers, N. R. Cook, T. Gerdts, M. Gonen, N. Obuchowski, M. J. Pencina, and M. W. Kattan, "Assessing the performance of prediction models: a framework for traditional and novel measures," *Epidemiology*, vol. 21, no. 1, pp. 128–138, 2010.
- [24] R. Valavi, J. Elith, J. J. Lahoz-Monfort, and G. Guillera-Arroita, "blockcv: An r package for generating spatially or environmentally separated folds for k-fold cross-validation of species distribution models," *Biorxiv*, p. 357798, 2018.
- [25] P. Schratz, J. Muenchow, E. Iturritxa, J. Richter, and A. Brenning, "Hyperparameter tuning and performance assessment of statistical and machine-learning algorithms using spatial data," *Ecological Modelling*, vol. 406, pp. 109–120, 2019.
- [26] S. L. Oh, Y. Hagiwara, U. Raghavendra, R. Yuvaraj, N. Arunkumar, M. Murugappan, and U. R. Acharya, "A deep learning approach for parkinson's disease diagnosis from eeg signals," *Neural Computing and Applications*, vol. 32, no. 15, pp. 10927–10933, 2020.
- [27] S. A. A. Shah, L. Zhang, and A. Bais, "Dynamical system based compact deep hybrid network for classification of parkinson disease related eeg signals," *Neural Networks*, vol. 130, pp. 75–84, 2020.
- [28] R. Yuvaraj, U. Rajendra Acharya, and Y. Hagiwara, "A novel parkinson's disease diagnosis index using higher-order spectra features in eeg signals," *Neural Computing and Applications*, vol. 30, no. 4, pp. 1225–1235, 2018.
- [29] Q. Zhang, R. Zhang, B. Zhu, J. Xiao, Y. Liu, X. Han, and Z. Wang, "Gepd: Gan-enhanced generalizable model for eeg-based detection of parkinson's disease," in *International Conference on Intelligent Computing*. Springer, 2025, pp. 311–322.
- [30] C. Williams, D. Weinhardt, J. Hewson, M. B. Płomecka, N. Langer, and S. Musslick, "Eeg-gan: A generative eeg augmentation toolkit for enhancing neural classification," *bioRxiv*, pp. 2025–06, 2025.
- [31] A. Singh, R. C. Cole, A. I. Espinoza, D. Brown, J. F. Cavanagh, and N. S. Narayanan, "Frontal theta and beta oscillations during lower-limb movement in parkinson's disease," *Clinical Neurophysiology*, vol. 131, no. 3, pp. 694–702, 2020.
- [32] M. Corporation, "Microsoft copilot: Ai companion for productivity and research," Online. Available: <https://copilot.microsoft.com>, 2025, accessed: Oct. 23, 2025. Developed by Microsoft as a large language model-based assistant for writing, coding, and research support.